Improvement of thermal stability and reduction of LiBH4/polymer host interaction of nanoconfined LiBH4 for reversible hydrogen storage

Praphatsorn Plerdsranoy[1], Nuntida Wiset[1], Chiara Minalese[2], Danial Laipple[3], Amedeo Marini[2], Thomas Klassen[3], Martin Dornheim[3], Rapee Gosalawit–Utke[*,1]

[1]School of Chemistry, Institute of Science, Suranaree University of Technology, Nakhon Ratchasima 30000, Thailand, Email: rapee.g@sut.ac.th

[2]Pavia Hydrogen Lab., C. S. G.I., Department of Chemistry, Physical Chemistry Division, University of Pavia, Pavia 27100, Italy.

[3]Institute of Materials Research, Helmholtz–Zentrum Geesthacht, Geesthacht 21502, Germany.

Improvement of thermal properties and reduction of hydride/polymer ($LiBH_4$/Poly (methyl methacrylate)–co–butyl methacrylate (PcB)) interaction of nanoconfined $LiBH_4$–PcB by doping with small amount of MWCNT and $NaAlH_4$ is proposed. The greater amount of gases desorbed during dehydrogenation at 120 ˚C due to polymer degradation, relating to thermal instability of PcB host, of nanoconfined $LiBH_4$–PcB is 64.3 % with respect to H_2 content, while those of nanoconfined samples doped with MWCNT and $NaAlH_4$ are only 9 and 7.9 %, respectively. The reduction of $LiBH_4$/PcB interaction of the nanoconfined samples, especially B---OCH_3 interaction formed between borohydride ($[BH_4]^-$) and methoxy (–OCH_3) group of PcB, is quantitatively evaluated by FTIR technique using the ratio of B–H stretching peak area with respect to that of C=O stretching (υ(B–H)/υ(C=O)). The more the υ(B–H)/υ(C=O) ratio, the lower the $LiBH_4$/PcB (B---OCH_3) interaction. It is found that by adding small amount of MWCNT and $NaAlH_4$, υ(B–H)/υ(C=O) ratio significantly increases up to 78 %. This is in agreement with B 1*s* XPS results, where the relative amount of B_xO_y (x/y=3) to $LiBH_4$ decreases after MWCNT and $NaAlH_4$ doping. It should be remarked that thermal stability improvement and decrease of $LiBH_4$/PcB interaction of nanoconfined $LiBH_4$–PcB are significantly accomplished after doping with MWCNT and $NaAlH_4$. These result in considerable amount of hydrogen release and uptake as well as hydrogen reproducibility efficiency during cycling as compared with unmodified nanoconfined $LiBH_4$–PcB; however, the dispersion of MWCNT is still one of the most critical factors to be concerned due to probably its hindrance for hydrogen diffusion.

Key words: thermal stability, polymer hosts, PMMA-co-BM, hydride-polymer interaction.
* Corresponding author

1. Introduction

On the basis of particle agglomeration of metal and complex hydrides upon hydrogen release and uptake cycles [1], leading to reduction in hydrogen diffusion and exchange rate, nanoconfinement in carbon aerogel scaffolds (CAS) have been recently of interest to constrain the particle size and maintain diffusion distances. One of the most promising complex hydrides frequently modified via nanoconfinement in CAS is lithium borohydride ($LiBH_4$) due to its high hydrogen storage capacity of 13.8 wt. % [2]. Confinement of $LiBH_4$ in nanoporous hard carbon with hexagonally packed 2 nm diameter columnar pores revealed significant reduction in onset dehydrogenation temperature of $LiBH_4$ (from 460 to 220 °C) and suppression of toxic diborane (B_2H_6) gas [3]. Afterwards, via loading CoNiB in nanoconfined $LiBH_4$, onset desorption temperature was further decreased to 192 °C as well as excellent desorption kinetics (9.33 wt. % H_2 in 30 min at 350 °C) [4]. Moreover, composite hydrides of $LiBH_4$ with other metal and complex hydrides ($LiBH_4$–MgH_2 [5], $LiBH_4$–$LiAlH_4$ [6], and $LiBH_4$–$Mg(BH_4)_2$ [7]) were nanoconfined in CAS mainly via melt infiltration technique. Nanoconfinement of $LiBH_4$–MgH_2 showed single–step dehydrogenation at lower onset temperature (ΔT=38–103 °C as compared with milled $LiBH_4$–MgH_2) as well as ten times faster kinetics with respect to milled material [5].

Recently, hydrogen permeable polymeric hosts for nanoconfinement of hydride materials were also reported [8–10]. For example, Pd or $LaNi_5$ (particle size of ~1 μm) were embedded into polyethylene (PE), polysiloxane (PS), and polyvinyl pyrolidone (PVP). $LaNi_5$–PS showed negligible H_2 storage capacity, while $LaNi_5$–PE, Pd–PS, and Pd–PVP were completely hydrogenated. It was found that no interaction between an activated metal surface and polymeric chains was observed; however, the slow kinetics and metal particle agglomeration in polymer matrix were detected [8]. Furthermore, Mg nanocrystals confined in poly methyl methacrylate (PMMA) enabled both high H_2 storage capacity (up to 6 wt. % H_2 at 200 °C) and rapid kinetics without using expensive heavy–metal catalysts [9]. Morover, Houng et al. [10] reported nanoconfinement of $LiBH_4$ in PMMA pore network structure, where the interaction between $LiBH_4$ and PMMA led to fast hydrogen release from $LiBH_4$ at low temperature (ΔT=237 °C as

compared with pure $LiBH_4$). Recently, our group reported nanoconfined $LiBH_4$ in a new host material of poly (methyl methacrylate)–co–butyl methacrylate (PMMA–co–BM), denoted as nano $LiBH_4$–PMMA–co–BM [11]. Long butyl branches of PMMA–co–BM providing superior amorphous degree and free volume to PMMA could benefit hydrogen permeability. The chemical structures of PMMA and PMMA–co–BM are compared and revealed in Schemes 1 (A) and (B), respectively. Nano $LiBH_4$–PMMA–co–BM started to desorb hydrogen at ~80 °C and 8.8 wt. % H_2 with respect to $LiBH_4$ content released within 4 h at 120°C under vacuum, while rehydrogenation was accomplished under considerably mild conditions of T = 140 °C, P (H_2) = 50 bar.

In the previous work [11], it was reported that thermal degradation of PMMA–co–BM polymer detected under temperature and pressure condition during cycling could result in ineffective nanoconfinement of $LiBH_4$ due to damaged host. Moreover, $LiBH_4$/polymer interaction, especially B---OCH_3 formed between borohydride ($[BH_4]^-$) and methoxy (–OCH_3) group of PMMA–co–BM, led to the reduction of $[BH_4]^-$ for dehydrogenation, resulting in deficient hydrogen content released. Therefore, in this work, we intend to improve the efficiency of nano $LiBH_4$–PMMA–co–BM via (i) thermal stability enhancement of PMMA–co–BM host, favorable for hydrogen reproducibility during cycling, and (ii) reduction of the interaction between $LiBH_4$ and PMMA–co–BM, leading to greater amount of hydrogen desorbed. It was reported that the addition of multi–walled carbon nanotube (MWCNT) could increase the glass transition (T_g), melting (T_m) and decomposition (T_d) temperatures of polymer matrix due to their constraint effect on the polymer segments and chains, for instance, 2 vol. % of MWCNT added into poly (propylene) (PP) could enhance decomposition temperature of PP by 12 °C [12–13]. To compromise the thermal stability, hydrogen permeability, and hydrogen storage capacity, in this work only 0.1 wt. % of MWCNT is added into nano $LiBH_4$–PMMA–co–BM. Regarding reduction of $LiBH_4$/polymer interaction, $NaAlH_4$, where $[AlH_4]^-$ could provide a competitive interaction with PMMA–co–BM, is slightly doped into nano $LiBH_4$–PMMA–co–BM. Moreover, $NaAlH_4$ can contribute catalytic effects to de/rehydrogenation of $LiBH_4$ [14–15].

2. Experimental details

2.1 Sample preparation

Tetrahydrofuran (THF) (HPLC grade, QRëC^{TM}) was pre–dried overnight by molecular sieves. Sodium metal (Na) and benzophenone of 5.0017 and 20.0006 g,

respectively, were added to 500.0 mL of pre–dried THF [16]. The mixture was refluxed under nitrogen atmosphere at 80 °C until a deep blue color was obtained. The mixture was distilled at 70 °C under nitrogen atmosphere to obtain anhydrous THF.

Poly (methyl methacrylate)–co–butyl methacrylate (PMMA–co–BM, M_w=75,000 g/mol, Sigma Aldrich), denoted shortly in this work as PcB, of 20.4890 g was dissolved in 100.0 mL anhydrous THF with continuous stirring to obtain homogeneous polymer solution (20.0 % w/v). The PcB solution was precipitated in distillated n–hexane (AR grade, QRëC^{TM}) and dried at 90 °C for 24 h in vacuum oven to obtained dried PcB polymer powder.

The PcB polymer solution was prepared by dissolving 5.0656 g of PcB polymer powder in 20.00 mL anhydrous THF with continuous stirring. Lithium borohydride ($LiBH_4$) solution (2 M in THF, Sigma Aldrich) of 15.00 mL was added to PcB polymer solution. The transparent gel was obtained after stirring the mixture of $LiBH_4$ and PcB for approximately 10 min at room temperature in the glove box. The gel was dried at room temperature in the glove box for several days to achieve nanoconfined sample of $LiBH_4$ in PcB (containing 11.53 wt. % of $LiBH_4$), denoted as nano $LiBH_4$–PcB. With respect to the $LiBH_4$ content, theoretical hydrogen storage capacity of 1.60 wt. % was achieved.

PcB polymer powder of 5.0745 g was dissolved in 20.00 mL anhydrous THF and stirred to obtain PcB polymer solution. Multi–walled carbon nanotube (MWCNT) of 0.0055 g (0.10 wt. % of MWCNT with respect to PcB content) was dispersed homogeneously in PcB polymer solution by using ultra sonication for several hours. The clear solution of PcB containing MWCNT was added with 10.00 mL $LiBH_4$ solution (2 M in THF, Sigma Aldrich) in the glove box and continuously stirred for approximately 10 min to obtain transparent gel. The gel was dried at room temperature in the glove box to obtain nanoconfined $LiBH_4$ in PcB−MWCNT (containing 8.00 wt. % of $LiBH_4$), denoted as nano $LiBH_4$–PcB–MWCNT. With respect to the $LiBH_4$ content, theoretical hydrogen storage capacity of 1.10 wt. % was obtained.

Sodium aluminium hydride ($NaAlH_4$, ≥93%, hydrogen storage grade, Sigma–Aldrich) powder of 0.3013 g was dissolved in 85.00 mL anhydrous THF and continuously stirred for several hours in the glove box to obtain $NaAlH_4$ solution (0.35 %w/v $NaAlH_4$ in THF). PcB polymer powder of 0.5144 g was dissolved in 5.00 mL anhydrous THF to obtain PcB polymer solution. The solutions of $LiBH_4$ (2 M in THF, Sigma Aldrich) and $NaAlH_4$ (0.35 %w/v in THF) of 1.50 and 2.00 mL, respectively, were

added into PcB polymer solution. The mixture was stirred for 1 h and transparent gel was achieved. The gel was dried at room temperature in the glove box for several days to achieve nanoconfined $LiBH_4$–$NaAlH_4$ in PcB (containing 11.2 and 1.2 wt. % of $LiBH_4$ and $NaAlH_4$, respectively), denoted as nano $LiBH_4$–$NaAlH_4$–PcB. On the basis of $LiBH_4$:$NaAlH_4$ molar ratio (10:0.5), only small amount of $NaAlH_4$ was added into the sample. Thus, $NaAlH_4$ was considered as an additive, where its H_2 storage capacity could be probably negligible. With respect to the $LiBH_4$ content, theoretical hydrogen storage capacity was calculated to be 1.55 wt. %.

2.2 Characterizations

De/rehydrogenation kinetics and hydrogen reproducibility of all nanoconfined samples were studied by using a laboratory scale setup of a carefully calibrated Sievert–type apparatus (Figure 1) [11]. The powder sample of ~50–100 mg was packed in a high pressure stainless steel sample holder (316SS, Swagelok) under argon atmosphere in the glove box, and transferred to the Sievert–type apparatus. Two K–type thermocouples (-250−1,300 °C, SL heater) were attached to the sample holder and to the furnace for measuring the temperature change of the system during de/rehydrogenation. Pressure transducers (C206, Cole Parmer) in the pressure range of 0–500 psig and 0–3000 psig were used to measure the pressure changes due to hydrogen desorption and absorption, respectively. Thermocouples and pressure transducers were connected to an AI210I module convertor data logger (from Wisco), measuring and transferring (every 1 s) the pressure and temperature changes of the sample to the computer for further evaluation. Dehydrogenation of the samples was done under an isothermal condition of 120 °C (vacuum) via a furnace controlled by a PID temperature controller. In the case of rehydrogenation, the dehydrogenated powder sample was pressurized under 60 bar H_2 (purity= 99.999 %) at 120 °C for 12 h. Once the pressure reading was constant over a period of time, the amount of hydrogen released was calculated by the pressure change (ΔP) and the following equations:

$$(\Delta P)V = nRT \quad (1)$$

$$H_2 \text{ desorbed (wt. \%)} = [(n \times 2.0158)/\text{sample weight}] \times 100 \quad (2)$$

where *P*, *V*, and *T* are hydrogen pressure (atm), volume of the system (L), and temperature (K), respectively, *n* is the number of hydrogen moles (mol), and *R* is gas constant (0.0821 L atm K^{-1} mol^{-1}).

The analyses of gases released during dehydrogenation of nano $LiBH_4$–PcB, $LiBH_4$–PcB–MWCNT, and $LiBH_4$–$NaAlH_4$–PcB were carried out by connecting a manometric PCTPro–2000 apparatus with a residual gas analyzer (RGA200, Setaram, France) by using a 1/8" stainless steel tube. The powder sample (~200 mg) was loaded in the sample holder and transferred to the PCTPro–2000 apparatus. The measurement was done by heating the powder sample from room temperature to 300 °C (5 °C/min) under vacuum.

Scanning electron microscopy (SEM) was carried out with an Auriga from Zeiss, Germany. Nano $LiBH_4$–PcB–MWCNT and $LiBH_4$–$NaAlH_4$–PcB were deposited on the sample holder by using silver glue (in *n*–butyl acetate). The powder samples were coated with platinum (Pt) by using sputtering technique with a current of 30 mA for 30 s under vacuum. An energy−dispersive X−ray spectroscopy (EDS)–elemental mapping were managed by an apparatus from EDAX Inc., USA. Smart SEM and EDS Genesis programs were used for morphological studies and elemental analysis of the samples, respectively.

Fourier transform infrared spectroscopy (FTIR) of standard samples ($LiBH_4$, $NaAlH_4$, PcB and PcB–MWCNT composite) and all nanoconfined samples at different stages of before and after dehydrogenation and after rehydrogenation were performed by using a Bruker, Model Tensor 27. The sample was ground with anhydrous KBr (1:10 weight ratio of sample:anhydrous KBr) and pressed under 3 tons for 2 min to obtain KBr pellet. FTIR spectrum of each sample was obtained by assembling KBr pellet containing the sample in the FTIR machine on the direction of infrared. The spectrum was recorded in the range of 4000–400 cm^{-1} with 32 scans at room temperature. The quantitative analysis from FTIR spectra was carried out by curve fitting technique using a Magic Plot program [11].

X–ray photoelectron spectroscopy (XPS) was carried out at the Siam Photon Laboratory, BL 3.2a, Synchrotron Light Research Institute (Public Organization), Ministry of Science and Technology, Thailand. The powder samples of pure $LiBH_4$ and nanoconfined samples of $LiBH_4$–PcB, $LiBH_4$–PcB–MWCNT, and $LiBH_4$–$NaAlH_4$–PcB were deposited on the sample holders by using carbon glue tape in the glove box

atmosphere. Prior to the measurements, all prepared samples were placed in an ultrahigh vacuum chamber for approximately 6 h. An aluminum–anode source, producing Al K_α (1638.4 eV) in an ultrahigh vacuum chamber ($1x10^{-10}$ mbar) was used as an X–ray source. The photon energy of 400 eV was used to detect the signals of Li 1*s* and B 1*s*. Each element was investigated at the kinetic energy step of 0.1 eV for 5 scans by using a CLAM2 analyzer (Thermo VG Scientific). The multi spectra were analyzed by using a macro XPS macro code developed in the Microsoft Excel Visual Basic for Applications.

Solid–state ^{11}B, ^{27}Al, and ^{23}Na magic angle spinning (MAS) nuclear magnetic resonance (NMR) spectra of nano $LiBH_4$–$NaAlH_4$–PcB were recorded by a Bruker ASCEND^{TM} 500 spectrometer using a BL4 VNT probe for 4 mm outer diameter rotors. The powder sample was tightly packed in a zirconia end–capped tube in the glove box, and solid–state MAS NMR measurements were carried out at 302 K. Solid–state MAS NMR experiments employed a rotation frequency of 10 kHz. The excitation pulse lengths of ^{11}B and ^{27}Al MAS NMR were 5 and 9.8 μs, respectively. The relaxation delays of ^{11}B, ^{27}Al, and ^{23}Na MAS NMR were comparable at 5 s. The ^{11}B, ^{27}Al, and ^{23}Na chemical shifts were detected in part per million (ppm) relative to neat boric acid (H_2BO_3), aluminium oxide (Al_2O_3), and sodium chloride (NaCl), respectively.

3. Results and discussion

To study dehydrogenation kinetics, reversibility, and hydrogen reproducibility, titration measurements of nanoconfined samples were performed by using Sievert–type apparatus. Dehydrogenation and rehydrogenation were carried out at the same temperature of 120 °C under vacuum and 60 bar H_2, respectively. With respect to the previous studies, PcB polymer matrix thermally degraded and produced gases during dehydrogenation at 120 ˚C under vacuum [11]. Thus, regarding the hydrogen contents desorbed during cycling in this study, titration results of nano $LiBH_4$–PcB and $LiBH_4$–$NaAlH_4$–PcB are subtracted by the amount of gases releasing due to thermal degradation of PcB (~0.04 wt. %) at 120 °C under vacuum for 6 h, while those of nano $LiBH_4$–PcB–MWCNT are subtracted by degradation of PcB–MWCNT composite (~0.01 wt. %) under the same temperature, pressure, and time condition. With respect to the amount of $LiBH_4$ in each sample, theoretical hydrogen storage capacities of 1.60, 1.10, and 1.55 wt. % H_2 are calculated for nano $LiBH_4$–PcB, $LiBH_4$–PcB–MWCNT, and $LiBH_4$–$NaAlH_4$–PcB, respectively (Table 1). From Figure 2 (A), nano $LiBH_4$–PcB released 0.78 wt. % H_2 (49

% of theoretical hydrogen storage capacity) during the 1st dehydrogenation within 4 h. The inferior hydrogen storage capacity to the theoretical value (1.60 wt. % H_2) can be due to the interaction between $LiBH_4$ and methoxy branches (–OCH_3) of PcB formed during sample preparation, discussed and reported in the previous studies [11]. For the 2nd cycle, nano $LiBH_4$–PcB provides only 0.32 wt. % H_2 (20 % of theoretical hydrogen storage capacity) (Figure 2 (A)). Significant reduction in hydrogen content released in the 2nd dehydrogenation with respect to the 1st cycle can be due to (i) greater interaction between $LiBH_4$ and PcB after cycling as previously reported [11] and (ii) thermal degradation of PcB polymer host during cycling under temperature and pressure. From Figure 2 (B), nano $LiBH_4$–PcB–MWCNT releases 0.53 and 0.41 wt. % H_2, that is, approximately 48 and 37 % of theoretical hydrogen storage capacity (1.10 wt. % H_2), respectively, within 6 h during the 1st and 2nd cycles, respectively. The deficient hydrogen storage capacity as compared with theoretical value can be due to the interaction between $LiBH_4$ and PcB polymer matrix, revealed as gel formation during sample preparation as in case of nano $LiBH_4$–PcB. Regarding dehydrogenation kinetics, slower hydrogen exchange reaction rate is obtained due to addition of MWCNT into nano $LiBH_4$–PcB (Figures 2 (A) and (B)). This could be due to the fact that the dispersion of MWCNT in nano $LiBH_4$–PcB probably obstructs and/or delays hydrogen diffusion pathway for de/rehydrogenation. However, it should be noted that the 2nd dehydrogenation of nano $LiBH_4$–PcB–MWCNT can preserve superior hydrogen content to that of nano $LiBH_4$–PcB, that is, up to 17 % of theoretical hydrogen storage capacity were additionally reproduced in the 2nd cycle by compositing nano $LiBH_4$–PcB with MWCNT. This could be due to the improvement of thermal stability of PcB host via compositing with MWCNT, further confirmed by gas analysis results (Figure 3). Furthermore, nano $LiBH_4$–$NaAlH_4$–PcB releases 1.23 and 0.64 wt. % H_2 (79 and 41 % of theoretical hydrogen storage capacity, respectively) during the 1st and 2nd dehydrogenations, respectively. It should be remarked that during the 1st cycle nano $LiBH_4$–$NaAlH_4$–PcB not only releases the highest content of hydrogen (79 % of theoretical hydrogen storage capacity) among other nanoconfined samples, but also provides the fastest dehydrogenation kinetics. For example, H_2 desorption of nano $LiBH_4$–$NaAlH_4$–PcB is complete within 1 h, while that of nano $LiBH_4$–PcB requires up to 4 h (Figures 2 (A) and (C)). For nano $LiBH_4$–PcB–MWCNT, its dehydrogenation still slightly proceeds after 6 h (Figure 2 (B)). Moreover, hydrogen content reproduced in the 2nd cycle of nano $LiBH_4$–$NaAlH_4$–PcB is the highest among all nanoconfined samples; for instance, nano $LiBH_4$–$NaAlH_4$–PcB gives 41 % of theoretical hydrogen storage

capacity, while those of nano $LiBH_4$–PcB and $LiBH_4$–PcB–MWCNT are 20 and 37.3 %, respectively. These imply that small amount of $NaAlH_4$ (10:0.5 mole ratio of $LiBH_4$:$NaAlH_4$) doped into nano $LiBH_4$–PcB significantly affects both thermal stability and interaction between $LiBH_4$ and PcB polymer matrix. Moreover, fast kinetics of nano $LiBH_4$–$NaAlH_4$–PcB could be due to the catalytic effects of $NaAlH_4$ on dehydrogenation of $LiBH_4$ as previously reported [14].

To confirm the effects of MWCNT and $NaAlH_4$ on thermal stability of nano $LiBH_4$–PcB, gas analyses of all nanoconfined samples were carried out in the temperature range of 30–300 ˚C (dT/dt = 5 ˚C/min). From Figure 3 (A), hydrogen is the main gas released from nano $LiBH_4$–PcB together with gases due to thermal degradation of PcB, that is, •CH_3, H_2O, CO, •OCH_3, CO_2, and •OC_4H_9 [11, 17–18]. Furthermore, the relative amount of each gas, representing by its peak area, at different temperatures was evaluated (Figure 3 (B)). Dehydrogenation of nano $LiBH_4$–PcB is found in the temperature range of 80–135 ˚C, where the main dehydrogenation (T_p) is at ~105 ˚C (Figure 3 (B) and Table 2), corresponding to the previous studies [11]. For thermal degradation of PcB, combination of gases (CO_2, CO, •OC_4H_9, •CH_3, and •OCH_3) are observed during dehydrogenation range (80–135 ˚C), and especially CO_2, •CH_3 and •OC_4H_9 are firstly detected approximately at onset dehydrogenation temperature (T_i) (~ 80 ˚C) (Figure 3 (B)). Regarding Figure 3 (B), the relative amounts of gases due to thermal degradation of PcB at 120 ˚C (dehydrogenation temperature used for titration measurements) from nano $LiBH_4$–PcB are totally 64.3 % with respect to hydrogen content released (Table 2). Moreover, significant amount of •CH_3 (59 % with respect to the highest content of hydrogen released) is detected at ~ 145 ˚C. Considerable amount of gases obtained from thermal degradation of PcB during dehydrogenation of nano $LiBH_4$–PcB hits at thermal instability of PcB host. For nano $LiBH_4$–PcB–MWCNT (Figure 3 (C)), hydrogen is the main gas desorbed together with other gases due to thermal degradation of PcB as in the case of nano $LiBH_4$–PcB (Figure 3 (A)). Dehydrogenation of nano $LiBH_4$–PcB–MWCNT proceeds in the temperature range of 85–190 ˚C, where the main desorption temperature (T_p) is at 130 ˚C (Figure 3 (D) and Table 2). At 120 ˚C (dehydrogenation temperature), total amount of gases desorbed due to thermal degradation of PcB is 9.0 % with respect to hydrogen content released. It should be noted that although dehydrogenation temperatures of nano $LiBH_4$–PcB increase after modifying with MWCNT (e.g., ΔT_p, ΔT_i, and ΔT_f are 5, 25, and 55 ˚C, respectively), thermal stability

improvement of PcB host at the same dehydrogenation temperature of 120 ˚C is considerably accomplished. Moreover, it is found that degradation of PcB in nano $LiBH_4$–PcB–MWCNT starts at 120 ˚C, approximately 40 ˚C higher than that of nano $LiBH_4$–PcB. Therefore, due to thermal stability improvement of PcB after compositing with MWCNT, hydrogen reproducibility in the 2nd cycle of nano $LiBH_4$–PcB–MWCNT is more effective than nano $LiBH_4$–PcB (Figures 2 (A) and (B)). In the case of nano $LiBH_4$–$NaAlH_4$–PcB, Figure 3 (E) reveals remarkable amount of hydrogen desorbed as well as other gases from partial thermal degradation of PcB as similar as other nanoconfined samples. Dehydrogenation of nano $LiBH_4$–$NaAlH_4$–PcB starts (T_i) and finishes (T_f) at 95 and 165 ˚C, respectively, while the main hydrogen desorption temperature (T_p) is at 125 ˚C (Figure 3 (F) and Table 2). Interestingly, the relative amount of gases desorbed with respect to hydrogen content at dehydrogenation temperature (120 ˚C) of nano $LiBH_4$–$NaAlH_4$–PcB, corresponding to thermal stability of PcB, is totally only 7.9 % (Table 2). Thus, by doping small amount of $NaAlH_4$ in nano $LiBH_4$–PcB, it results in significant improvement in thermal stability of PcB host, corresponding to significant amount of hydrogen reproduced in the 2nd cycle (Figure 2 (C)). It was reported that thermal stability of polymers could be improved by compositing with metal or metal ion. For instance, polystyrene–block–poly(2–vinylpyridine) (PS–b–P2VP) compositing with metal or metal ion (Co, Cr, and Au^{3+}) revealed that the more the interaction between polymer and metal (or metal ion), the higher the thermal stability [19]. Regarding nano $LiBH_4$–$NaAlH_4$–PcB, not only polymer–ion interaction at carbonyl (C=O) groups of PcB with Li^+ ion (from $LiBH_4$) is observed as in case of nanoconfined $LiBH_4$–PcB [11], but also that with Na^+ ion (from $NaAlH_4$) is probably achieved.

Furthermore, morphology and elemental distribution of nano $LiBH_4$–PcB–MWCNT and $LiBH_4$–$NaAlH_4$–PcB were studied by SEM–EDS–mapping technique. Figure 4 (A) shows sample morphology of nano $LiBH_4$–PcB–MWCNT, where elemental analysis and mapping were taken into account. From Figures 4 (B) and (C), homogeneous distribution of boron (B) and carbon (C) from $LiBH_4$ and PcB (as well as MWCNT), respectively, are observed. In addition, Figure 4 (C) reveals the bright–green line along the edge of sample bulk, probably representing the agglomeration of carbon from MWCNT. It was previously reported that good distribution of MWCNT in poly(methyl methacrylate) (PMMA) polymer matrix, which can be achieved by surface modification of MWCNT with some functional groups, such as alkyl silane [20], amine

and carboxyl groups [21], encouraged thermal stability of PMMA [22]. From our work, although partial agglomeration of MWCNT is found in nano $LiBH_4$–PcB–MWCNT (Figure 4 (C)), up to 88 % increase of thermal stability, calculated from total amount of gases desorbed with respect to H_2 content at dehydrogenation temperature (120 °C) of nano $LiBH_4$–PcB (64.3 %) and $LiBH_4$–PcB–MWCNT (9.0 %) (Table 2), is accomplished. Figure 4(D) exhibits the signals of C (from PcB and MWCNT) and oxygen (O) (from PcB) as the main elements together with B from $LiBH_4$. In the case of lithium (Li) from $LiBH_4$, it cannot be detected due to the limitation of EDS technique to light elements. For nano $LiBH_4$–$NaAlH_4$–PcB, SEM image, where the elemental mapping and analysis are studied, is shown in Figure 5 (A). Good distribution of C, B, aluminium (Al), and sodium (Na) from PcB, $LiBH_4$, and $NaAlH_4$, respectively, is observed (Figures 5 (B), (C), (D), and (E)). Furthermore, signals of all mapped elements (B, C, Na, and Al) as well as O and platinum (Pt) from PcB and surface coating, respectively, are quantitatively determined and shown in Figure 5 (F).

Afterwards, reversibility of all nanoconfined samples was confirmed by FTIR technique. Prior to FTIR investigation of nanoconfined samples, all standard samples ($LiBH_4$, $NaAlH_4$, PcB, and composite of PcB and MWCNT) related to nanoconfined samples are determined. Pristine $LiBH_4$ reveals vibrational peaks of B–H stretching at 2395, 2298, and 2234 cm^{-1} and bending at 1125 cm^{-1} (Figure 6 (a)). The peak at 1640 cm^{-1} refers to O–H bond from the contamination of moisture in air during the experiments [11]. $NaAlH_4$ exhibits characteristic peaks of Al–H stretching and bending at 1652 and 887 cm^{-1}, respectively, (Figure 6 (b)) approaching to the previous report [23]. For PcB, vibrational peaks corresponding to C–H stretching are observed at 2992 and 2956 cm^{-1}, while that of C=O stretching is at 1730 cm^{-1} (Figure 6 (c)) [24]. The absorption peaks at around 1486 and 1443 cm^{-1} belong to asymmetric bending vibration of C–CH_2 and C–CH_3 bonds, respectively, whereas the two peaks at 1387 and 752 cm^{-1} attribute to the α–methyl group vibration [24]. The two doublet bands at 1273–1242 and 1196–1154 cm^{-1} refer to C–O stretching of ester group. The vibrational peaks of main chain C–C stretching and C=O deformation are at 988–963 and 838 cm^{-1}, respectively [25]. In the case of PcB compositing with 0.1 wt. % MWCNT, all characteristic peaks are similar to those of PcB, suggesting no chemical interaction between MWCNT and PcB (Figure 6 (d)). Therefore, thermal stability improvement of nano $LiBH_4$–PcB after compositing

with MWCNT, is physically achieved due to the constraint effect on the polymer segments and chains based on inorganic–polymer composite principle [13].

From Figure 7 (A), nano $LiBH_4$–PcB shows characteristic peaks of both $LiBH_4$ and PcB, suggesting the presence of $LiBH_4$ in PcB polymer matrix as previously reported [11]. In addition, a sharp peak at 1383 cm^{-1} and a shoulder at 1707 cm^{-1}, corresponding to the interactions between $LiBH_4$ and PcB, that is, B---OCH_3 and Li^+---O=C, respectively, are detected (Figure 7 (A)) [11]. After dehydrogenation, the characteristic peaks of PcB are still observed, while those of $LiBH_4$ disappear, suggesting complete dehydrogenation (Figure 7 (A)). In the case of rehydrogenated sample, recovery of partial $LiBH_4$ is found as shown as slight signals of B–H stretching and bending peaks (Figure 7 (A)). For nano $LiBH_4$–PcB–MWCNT and $LiBH_4$–$NaAlH_4$–PcB, vibrational peaks of B–H stretching (2386, 2293, and 2226 cm^{-1}) and bending (1127 cm^{-1}) of $LiBH_4$ are significantly detected together with those of PcB in the samples before desorption (Figures 7 (B) and (C)). A small shoulder at ~1708 cm^{-1} observed in nano $LiBH_4$–PcB–MWCNT (the spectrum before desorption in Figure 7 (B)) refers to Li^+----O=C interaction formed between $LiBH_4$ and PcB as in case of nano $LiBH_4$–PcB. In the case of nano $LiBH_4$–$NaAlH_4$–PcB, it should be noted that the shoulder at 1709 cm^{-1} belongs not only to Li^+----O=C interaction (between $LiBH_4$ and PcB), but also probably to Na^+----O=C interaction generated between $NaAlH_4$ and PcB (the spectrum before desorption in Figure 7 (C)). Regarding the sample before desorption of nano $LiBH_4$–PcB (Figure 7 (A)), vibrational peak of B–O bonds from B---OCH_3 interaction is confirmed by the sharp peak at 1383 cm^{-1}; however, for nano $LiBH_4$–PcB–MWCNT and $LiBH_4$–$NaAlH_4$–PcB, there is only a small broad peak at this wavenumber (spectra before desorption in Figures 7 (B) and (C)). Together with a peak at 752 cm^{-1}, the small peak at 1383 cm^{-1} of nano $LiBH_4$–PcB–MWCNT and $LiBH_4$–$NaAlH_4$–PcB attributes mainly to characteristic vibrational peak of α–methyl group in PcB (Figure 6 (C)). Regarding insignificant signal of B---OCH_3 interaction and considerably vibrational peak of B–H bonds of nano $LiBH_4$–PcB–MWCNT and $LiBH_4$–$NaAlH_4$–PcB, it should be remarked that by adding small amount of MWCNT and $NaAlH_4$, the interaction between $[BH]_4^-$ and –OCH_3 (B---OCH_3) can be reduced. This leads to significant amount of hydrogen release during the 1st dehydrogenation, especially from nano $LiBH_4$–$NaAlH_4$–PcB as compared with that of nano $LiBH_4$–PcB (Figures 2 (A) and (C)). For nano $LiBH_4$–PcB–MWCNT, the slow

kinetics could be due to the fact that MWCNT probably obstructs hydrogen diffusion through the PcB polymer matrix as previously discussed.

After dehydrogenation, nano $LiBH_4$–PcB–MWCNT reveals all vibrational peaks of PcB and slight signals of B–H stretching, hinting at incomplete dehydrogenation of $LiBH_4$ (spectrum after dehydrogenation in Figure 7 (B)). This could be due to the fact that dehydrogenation time of 6 h as in the titration result (Figure 2 (B)) is not enough to complete dehydrogenation. As previously discussed, although thermal stability improvement of PcB and reduction of $LiBH_4$/PcB interaction, confirmed by gas analyses and FTIR results, respectively, are obtained by adding small amount of MWCNT into nano $LiBH_4$–PcB, slow dehydrogenation kinetics is detected due to the inefficient hydrogen diffusion in the PcB matrix dispersed with MWCNT. In the case of nano $LiBH_4$–$NaAlH_4$–PcB, all vibrational peaks of PcB with no peaks corresponding to $[BH_4]^-$ are observed, suggesting complete dehydrogenation of $LiBH_4$ (spectrum after dehydrogenation in Figure 7 (C)). Afterwards, the FTIR spectra of nano $LiBH_4$–PcB–MWCNT and $LiBH_4$–$NaAlH_4$–PcB after rehydrogenation were studied to confirm reversibility of $LiBH_4$. Both nano $LiBH_4$–PcB–MWCNT and $LiBH_4$–$NaAlH_4$–PcB show B–H signals of $LiBH_4$, hinting at reversibility of $LiBH_4$ (spectrum after absorption in Figures 7 (B) and (C)). Owing to the significant signal of B–H stretching obtained after rehydrogenation as compared with that after dehydrogenation of nano $LiBH_4$–PcB–MWCNT (Figure 7 (B)), $LiBH_4$ is achieved mainly from reversibility, instead of the rest from dehydrogenation.

In order to quantitatively determine the reduction of $LiBH_4$/PcB interaction especially B---OCH_3 interaction, mainly resulting in loss of $[BH]_4^-$ for hydrogen desorption, FTIR spectra of all nanooconfined samples are considered. Because the strength of IR absorption is proportional to the concentration, FTIR technique can be used for quantitative analysis, practically reported in the form of relative concentration (or amount) between the phase of interest to the reference [26–27]. In this work, our phase of interest and reference are B–H (from $[BH_4]^-$) and C=O (from PcB) stretching peaks, respectively. The more the IR absorption signal, represented by the peak area, of B–H stretching (υ(B–H)) with respect to that of C=O stretching (υ(C=O)), the lower B---OCH_3 interaction. The peak areas of υ(B–H) (in the range of 2386–2226 cm^{-1}) and υ(C=O) (at 1730 cm^{-1} and the shoulder due to Li^+/Na^+---O=C interaction at 1710–1708 cm^{-1}) were calculated by curve fitting method using Magic Plot program (Figure 8).

Figure 8 exhibiting curve fitting of FTIR spectra from all nanoconfined samples (before dehydrogenation) reveal goodness of fit due to high R^2 values (0.98–0.99). The peak area of both vibrations (υ(B–H) and υ(C=O)) as well as the ratio of the peak area (υ(B–H)/υ(C=O)) calculated from Figure 8 are summarized in Table 3. Nano $LiBH_4$–PcB, $LiBH_4$–PcB–MWCNT, and $LiBH_4$–$NaAlH_4$–PcB reveal υ(B–H)/υ(C=O) ratio of 0.6, 2.7, and 2.8, respectively (Figure 8 and Table 3). Due to the lowest υ(B–H)/υ(C=O) ratio (0.6), it is clear that nano $LiBH_4$–PcB has the highest content of B---OCH_3 interaction among other nanoconfined samples. Therefore, it can be claimed that MWCNT and $NaAlH_4$ significantly reduces $LiBH_4$/PcB interaction. Regarding the titration measurements during the 1st cycle (Figures 2 (A) and (C)), greater amount of hydrogen content released from nano $LiBH_4$–$NaAlH_4$–PcB as compared with that of nano $LiBH_4$–PcB can be due to the reduction of B---OCH_3 interaction. The reduction of $LiBH_4$/PcB interaction in case of nano $LiBH_4$–$NaAlH_4$–PcB could be explained by the fact that the interaction of $[AlH_4]^-$ (from $NaAlH_4$) to alkoxy (–OCH_3 and/or –OC_4H_9) groups of PcB, competing to B---OCH_3 interaction of $LiBH_4$ and PcB, provides free $[BH_4]^-$ for dehydrogenation. The interaction between $[AlH_4]^-$ and –OCH_3 (and/or –OC_4H_9) is further proven and discussed by solid state MAS NMR results. In the case of nano $LiBH_4$–PcB–MWCNT, although its υ(B–H)/υ(C=O) ratio (2.7) is higher than that of nano $LiBH_4$–PcB (0.6), the deficient amount of hydrogen content desorbed and slow kinetics are detected in the same dehydrogenation time range (6 h). This can be explained that the dispersion of MWCNT not only physically hindrances $LiBH_4$/PcB interaction, but also probably obstructs hydrogen diffusion through the sample bulk. Thus, although thermal stability and $LiBH_4$/PcB interaction can be altered by adding MWCNT, the dispersion of MWCNT in nanoconfined sample bulk should be significantly taken into account.

Furthermore, XPS of neat $LiBH_4$ and all nanoconfined samples were carried out to confirm that the deterioration of $LiBH_4$ could be avoided by nanoconfinement in PcB (nano $LiBH_4$–PCB) and in modified PcB (nano $LiBH_4$–PcB–MWCNT and $LiBH_4$–$NaAlH_4$–PCB). Also, the reduction of $LiBH_4$/PcB (B---OCH_3) interaction after adding MWCNT and $NaAlH_4$ into nano $LiBH_4$–PCB can be determined by XPS technique. From Figure 9 (a), Li 1*s* XPS spectrum of bulk $LiBH_4$ shows the characteristic peaks of Li_2O at 55 eV [28]. In the case of B 1*s*, the formations of B_xO_y (x/y = 3) and B_2O_3 are observed at 187 and 192 eV [29], respectively. The formations of Li_2O, B_xO_y (x/y = 3)

and B_2O_3 suggest the reaction of $LiBH_4$ with oxygen and/or humidity in air, confirming instability of $LiBH_4$ in ambient condition (25 °C under atmospheric pressure) in accordance with previous report [11]. In the case of all nanoconfined samples, prior to the XPS experiments the samples were left in ambient environment (25 °C under atmospheric pressure) for 3 days. From Figures 9 (b), (c), and (d), all nanoconfined samples reveal Li 1*s* spectrum of $LiBH_4$ and LiH at 56 [29] and 54 [30] eV, respectively. The signal of $LiBH_4$ found in all nanoconfined samples attributes to the ability of PcB polymer matrix to prevent deterioration of $LiBH_4$ by oxidation with oxygen and humidity. In the case of LiH formation, it can be explained by partial dehydrogenation of $LiBH_4$ during nanoconfinement, in accordance with the inferior hydrogen content released to theoretical value during the 1st dehydrogenation (Figure 2). Regarding B 1*s* spectra, all nanoconfined samples show two peaks at 187 and 188 eV, implying $LiBH_4$ and B_xO_y (x/y = 3), respectively [29]. The signal of B_xO_y (x/y = 3) hints at the interaction between $[BH_4]^-$ and $–OCH_3$ of PcB (B---OCH_3) together with partial dehydrogenation of $LiBH_4$, in accordance with the formation of LiH (Li 1*s* XPS results) [11]. However, it should be remarked that the relative amounts of B_xO_y (from B---OCH_3 interaction) with respect to $LiBH_4$ obtained from nano $LiBH_4$–PcB–MWCNT and $LiBH_4$–$NaAlH_4$–PcB are considerably lower than that of nano $LiBH_4$–PcB (B 1*s* spectra in Figures 9 (b), (c), and (d)), suggesting the reduction of $LiBH_4$/PcB interaction after doping MWCNT and $NaAlH_4$ into nano $LiBH_4$–PcB. This is in agreement with FTIR and curve fitting results (Figure 8).

To further confirm the interaction between $[AlH_4]^-$ and alkoxy ($–OCH_3$ and/or $–OC_4H_9$) groups of PcB polymer matrix in nano $LiBH_4$–$NaAlH_4$–PcB, solid state ^{11}B, ^{27}Al, and ^{23}Na MAS NMR measurements were carried out. From Figure 10, ^{11}B MAS NMR spectrum of pristine $LiBH_4$ shows a single peak at -41.5 ppm [31], while that of nano $LiBH_4$–$NaAlH_4$–PcB gives the peak centered at -41.5 ppm with a shoulder at -42.7 ppm, corresponding to $LiBH_4$ and $NaBH_4$ [32], respectively. This suggests slight reaction between $LiBH_4$ and $NaAlH_4$ to produce $NaBH_4$ during sample preparation. Moreover, the peaks of B–O bonds found in the range of 0–20 ppm [33], especially the main peak at 0.4 ppm corresponding to BO_4 [34–35], are also detected in nano $LiBH_4$–$NaAlH_4$–PcB. This hints at the B---OCH_3 interaction between $LiBH_4$ and PcB polymer matrix, corresponding to B 1*s* XPS result (Figure 9 (d)). For ^{27}Al MAS NMR, $NaAlH_4$ shows a single peak at 95.6 ppm, approaching to the previous report [36]. In the case of nano $LiBH_4$–$NaAlH_4$–PcB, the signal of $NaAlH_4$ is observed (at 95.6 ppm) together with those

of aluminium alkoxide $[Al(OR)_3]_n$, where R could be either metyl ($–CH_3$) or butyl ($–C_4H_9$) groups of PcB polymer branches, at 50.1 and 43.6 ppm [37]. Therefore, it can be confirmed that there is not only B---OCH_3 interaction formed in nano $LiBH_4$–$NaAlH_4$–PcB, but also that of Al---OCH_3 and/or Al---OC_4H_9 is accomplished. Due to the interaction between $[AlH_4]^-$ and PcB (Al---OCH_3 and/or Al---OC_4H_9), B---OCH_3 interaction (between $LiBH_4$ and PcB) can be reduced, leading to increase of free $[BH_4]^-$ and greater content of hydrogen release. This is in agreement with titration, FTIR, and B 1*s* XPS results (Figures 2, 7, 8, and 9), where the amount of hydrogen desorbed and $[BH_4]^-$ signal obtained from nano $LiBH_4$–$NaAlH_4$–PcB are significantly higher than those of nano $LiBH_4$–PcB. Also, a small shoulder at 21.6 ppm, belonging to β–AlH_3 [38], is detected (^{27}Al MAS NMR in Figure 10). For ^{23}Na MAS NMR, pure $NaAlH_4$ reveals a single peak at -9.6 ppm [36], while that of nano $LiBH_4$–$NaAlH_4$–PcB also gives the main peak centered at -9.6 ppm (Figure 10). Therefore, by adding the small amount of $NaAlH_4$ in nano $LiBH_4$–PcB, $[AlH_4]^-$ interacts with $–OCH_3$ and/or $–OC_4H_9$ of PcB (Al---OCH_3 and/or Al---OC_4H_9), resulting in the reduction of $LiBH_4$/PcB interaction. In addition, residual $NaAlH_4$ is found together with new hydride phase of β–AlH_3.

4. Conclusion

In the present work, the efficiency of nanoconfined $LiBH_4$ in poly (methyl methacrylate)–co–butyl methacrylate (PcB) as reversible hydrogen storage based on enhancement of thermal stability and reduction of $LiBH_4$/PcB interaction was developed by doping with small amount of multi–wall carbon nanotube (MWCNT) and $NaAlH_4$ to produce nano $LiBH_4$–PcB–MWCNT and $LiBH_4$–$NaAlH_4$–PcB, respectively. The total amount of gases desorbed due to thermal degradation of PcB at 120 ˚C (dehydrogenation temperature) from nano $LiBH_4$–PcB was 64.3 % with respect to H_2 content, while those of nano $LiBH_4$–PcB–MWCNT and $LiBH_4$–$NaAlH_4$–PcB were only 9 and 7.9 %, respectively. In the case of $LiBH_4$/PcB interaction analyzed quantitatively by using FTIR technique, the ratio of the peak area between B–H stretching (from $LiBH_4$) and C=O stretching (from PcB) (υ(B–H)/υ(C=O)) of all nanoconfined samples, corresponding to the relative amount of $[BH_4]^-$ with respect to PcB, was determined. The more the υ(B–H)/υ(C=O) ratio, the higher the free $[BH_4]^-$ content, hinting at the lower the $LiBH_4$/PcB interaction. The ratio of υ(B–H)/υ(C=O) obtained from nano $LiBH_4$–PcB was 0.6, whereas those of nano $LiBH_4$–PcB–MWCNT and $LiBH_4$–$NaAlH_4$–PcB were 2.7 and 2.8,

respectively. Therefore, it could be claimed that by adding small amount of MWCNT and $NaAlH_4$, υ(B–H)/υ(C=O) ratio significantly increased up to 78 %. In addition, B 1*s* XPS results revealed that the relative amount of B_xO_y (from B---OCH_3 interaction) with respect to $LiBH_4$ obtained from nano $LiBH_4$–PcB–MWCNT and $LiBH_4$–$NaAlH_4$–PcB were considerably lower than that of nano $LiBH_4$–PcB, suggesting the reduction of $LiBH_4$/PcB interaction after doping with MWCNT and $NaAlH_4$. Although, MWCNT doped into nano $LiBH_4$–PcB improved thermal stability and reduced $LiBH_4$/PcB interaction, dehydrogenation kinetics was sluggish probably due to the fact that the dispersion of MWCNT hindered hydrogen diffusion in the sample bulk. Therefore, the dispersion of MWCNT was remarkably considered for further development of this hydrogen storage material. For nano $LiBH_4$–$NaAlH_4$–PcB, thermal stability could be developed due to the greater interaction between metal ions (Li^+ and Na^+) and carbonyl group (C=O) of PcB, while $LiBH_4$/PcB interaction was decreased by the competitive reaction of $[AlH_4]^-$ (from $NaAlH_4$) with –OCH_3 and/or –OC_4H_9 (from PcB).

5. Acknowledgements

The authors would like to acknowledge National Research Council of Thailand (project: SUT1–102–56–18–25) and Suranaree University of Technology for financial support. We also would like to thank Dr. Hideki Nakajima and Mr. Thanit Saisopa (BL 3.2a: PES, Synchrotron Light Research Institute, Thailand) for technical help and suggestions during XPS measurements as well as Dr. Yanling Hua (The Centre for Scientific and Technological Equipment, Suranaree University of Technology, Thailand) for solid state MAS NMR measurements.

6. Table and Figure captions

Table 1. Amount of all components and theoretical hydrogen storage capacity.

Table 2. Dehydrogenation temperatures and amount of gases desorbed with respect to H_2 content at 120 ˚C.

Table 3. Peak area of B–H stretching (υ(B–H)) and C=O stretching (υ(C=O)), obtained from curve fitting technique, as well as υ(B–H)/υ(C=O) ratio of all nanoconfined samples.

Figure 1. Schematic diagram of a laboratory scale Sievert–type apparatus.

Figure 2. Dehydrogenation kinetics during the 1st and 2nd cycles at 120 °C under vacuum of nano $LiBH_4$−PcB (A), nano $LiBH_4$–PcB–MWCNT (B), and nano $LiBH_4$–$NaAlH_4$–PcB (C).

Figure 3. Gas analysis during dehydrogenation (30–300 °C (5 °C/min) under dynamic vacuum) and relative amount of each gas at different temperatures of nano $LiBH_4$–PcB ((A) and (B), respectively), nano $LiBH_4$–PcB–MWCNT ((C) and (D), respectively), and nano $LiBH_4$–$NaAlH_4$–PcB ((E) and (F), respectively).

Figure 4. SEM image of nano $LiBH_4$–PcB–MWCNT (A), boron mapping mode (B), carbon mapping mode (C), and elemental analysis (D).

Figure 5. SEM image of nano $LiBH_4$–$NaAlH_4$–PcB (A), carbon mapping mode (B), boron mapping mode (C), aluminium mapping mode (D), sodium mapping mode (E), and elemental analysis (F).

Figure 6. FTIR spectra of bulk $LiBH_4$ (a), $NaAlH_4$ (b), PcB (c), and PcB–MWCNT composite (d).

Figure 7. FTIR spectra before and after hydrogen desorption and after hydrogen absorption of nano $LiBH_4$−PcB (A), nano $LiBH_4$–PcB–MWCNT (B), and nano $LiBH_4$–$NaAlH_4$–PcB (C).

Figure 8. Curve fitting of B−H and C=O stretching peaks (from FTIR spectra) of all nanoconfined samples.

Figure 9. Li 1*s* and B 1*s* XPS spectra of bulk $LiBH_4$ (a), nano $LiBH_4$−PcB (b), nano $LiBH_4$–PcB–MWCNT (c), and nano $LiBH_4$–$NaAlH_4$–PcB (d).

Figure 10. Solid state ^{11}B, ^{27}Al, and ^{23}Na MAS NMR of $LiBH_4$, $NaAlH_4$, and nano $LiBH_4$–$NaAlH_4$–PcB (a).

References

[1] Liu BH, Zhang BJ, Jiang Y. Hydrogen storage performance of $LiBH_4$+1/2MgH_2 composites improved by Ce–based additives. Int J Hydrogen Energy 2011; 36: 5418–24.

[2] Cahen S, Eymery JB, Janot R, Tarascon JM. Improvement of the $LiBH_4$ hydrogen desorption by inclusion into mesoporous carbons. J Power Sources 2009; 189:902–8.

[3] Liu X, Peaslee D, Jost CZ, Majzoub EH. Controlling the Decomposition Pathway of $LiBH_4$ via Confinement in Highly Ordered Nanoporous Carbon. J Phys Chem C 2010; 114: 14036–41.

[4] Zhao Y, Jiao L, Liu Y, Guo L, Li L, Liu H, et al. A synergistic effect between nanoconfinement of carbon aerogels and catalysis of CoNiB nanoparticles on dehydrogenation of $LiBH_4$. Int J Hydrogen Energy 2014; 39: 917–26.

[5] Gosalawite–Utke R, Nielsen TK, Saldan I, Laipple D, Cerenius Y, Jensen TR, et al. Nanoconfined 2$LiBH_4$–MgH_2 prepared by direct melt infiltration into nanoporous materials. J Phys Chem C 2011; 115:10903–10.

[6] Xia G, Meng Q, Guo Z, Gu Q, Liu H, Liu Z, et al. Nanoconfinement significantly improves the thermodynamics and kinetics of co–infiltrated 2$LiBH_4$–$LiAlH_4$ composites: Stable reversibility of hydrogen absorption/resorption. Acta Mater 2013; 61: 6882–93.

[7] Javadian P, Jensen TR. Enhanced hydrogen reversibility of nanoconfined $LiBH_4$–$Mg(BH_4)_2$. Int J Hydrogen Energy 2014; 39: 9871–6.

[8] Checchetto R, Bazzanella N, Miotello A, Carotenuto G, Nicolais L. Hydrogen sorption in metal–polymer composites: the role of interfaces. J Appl Phys 2009; 105: 083513.

[9] Jeon KJ, Moon HR, Ruminski AM, Jiang B, Kisielowski C, Bardhan R, et al. Air–stable magnesium nanocomposites provide rapid and high–capacity hydrogen storage without using heavy–metal catalysts. Nat Mater 2011; 10: 286–90.

[10] Huang J, Yan Y, Ouyang L, Wang H, Liu J, Zhu M. Increased air stability and decreased dehydrogenation temperature of $LiBH_4$ via modification within poly(methyl methacrylate). Dalton Trans 2014; 43: 410–3.

[11] Gosalawit–Utke R, Meethom S, Pistidda C, Milanese C, Laipple D, Saisopa T, et al. Destabilization of $LiBH_4$ by nanoconfinement in PMMA–co–BM polymer matrix for reversible hydrogen storage. Int J Hydrogen Energy 2014; 39: 5019–29.

[12] Swain SK, Jena I. Polymer/carbon nanotube nanocomposites: A novel material. Asian J Chem 2010; 22: 1–15.

[13] Kashiwagi T, Grulke E, Hilding J, Harris R, Awad W, Douglas J. Thermal Degradation and Flammability Properties of Poly(propylene)/Carbon Nanotube Composites. Macromol Rapid Commun 2002; 23: 761–5.

[14] Shi Q, Yu X, Feidenhans R, Vegge T. Destabilized $LiBH_4$–$NaAlH_4$ Mixtures Doped with Titanium Based Catalysts. J Phys Chem C 2008; 112: 18244–8.

[15] Ravnsbæk DB, Jensen TR. Tuning hydrogen storage properties and reactivity: Investigation of the $LiBH_4$–$NaAlH_4$ system. J Phys Chem Solids 2010; 71: 1144–9.

[16] Schwartz AM. The Benzophenone/Ketyl Tetrahydrofuran (THF) Still. Chem Eng News 1978; 24: 88.

[17] Kashiwagi T, Inaba A, Brown EJ, Hatada K, Kitayama T, Masuda E. Effects of weak linkages on the thermal and oxidative degradation of poly(methyl methacrylates). Macromolecules 1986; 19: 2160–8.

[18] Kashiwagi T, Inaba A, Hamins A. Behavior of primary radicals during thermal degradation of poly(methyl methacrylate). Polym Degrad Stab 1989; 26: 161–84.

[19] Lekesiz TO, Kaleli K, Uyar T, Kayran C, Hacaloglu J. Preparation and characterization of polystyrene–b–poly(2–vinylpyridine) coordinated to metal or metal ion nanoparticles. J Anal Appl Pyrol 2014; 106: 81–5.

[20] Yuen SM, Ma CCM, Chiang CL, Chang JA, Huang SW, Chen SC, et al. Silane–modified MWCNT/PMMA composites–Preparation, electrical resistivity, thermal conductivity, and thermal stability. Composites 2007; 38: 2527–35.

[21] Ormsby R, McNally T, Mitchell C, Halley P, Martin D, Nicholson T, et al. Effect of MWCNT addition on thermal and rheological properties of polymethy metharylate bone cement. Carbon 2011; 49: 2893–904.

[22] Jin Z, Pramoda KP, Xu G, Goh SH. Dynamic mechanical behavior of melt–processed multi–walled carbon nanotube/poly(methyl methacrylate) composites. Chem Phys Lett 2001; 337: 43–7.

[23] Xuanhui Q, Ping L, Zhang L, Qi W, Iqbal MZ, Rafique MY, et al. Superior Catalytic Effects of Nb_2O_5, TiO_2, and Cr_2O_3 Nanoparticles in Improving the Hydrogen Sorption Properties of $NaAlH_4$. J Phys Chem C 2012; 116: 11924–38.

[24] Duan G, Zhang C, Li A, Yang X, Lu L, Wang X. Preparation and Characterization of Mesoporous Zirconia Made by Using a Poly (methyl methacrylate) Template. Nanoscale Res Lett 2008; 3: 118–22.

[25] Matsushita A, Ren Y, Matsukawa K, Inoue H, Minami Y, Noda I, et al. Two–dimensional Fourier–transform Raman and near–infrared correlation spectroscopy studies of poly(methyl methacrylate) blends1. Immiscible blends of poly(methyl methacrylate) and atactic polystyrene. Vib Spec 2000; 24: 171–80.

[26] Pierce JA, Jackson RS, Van Every KW, Griffiths PR, Gao H. Combined deconvolution and curve fitting for quantitative analysis of unresolved spectral bands. Anal Chem 1990; 62: 477–84.

[27] Xiong Y, Chen G, Guo S, Li G. Lifetime prediction on NBR composite sheet in aviation kerosene by using nonlinear curve fitting of ATR–FTIR spectra. J Ind Eng Chem 2013; 19: 1611–6.

[28] http://srdata.nist.gov/xps/Default.aspx.

[29] Deprez E, Munoz–Marquez MA, Jimenez de Haro MC, Palomares FJ, Soria F, Dornheim M, et al. Combined x−ray photoelectron spectroscopy and scanning electron microscope studied of the $LiBH_4$−MgH_2 reactive hydride composite with and without a Ti−based additive. J Appl Phys 2011; 109: 014913.

[30] Fang ZZ, Kang XD, Yang ZX, Walker GS, Wang P. Combined Effects of Functional Cation and Anion on the Reversible Dehydrogenation of $LiBH_4$. J Phys Chem C 2011; 115: 11839−45.

[31] Choi YJ, Sohn HY, Fang ZZ, Kim C, Bowman, Jr RC, et al. Reaction Mechanisms in the Li_3AlH_6/$LiBH_4$ and Al/$LiBH_4$ Systems for Reversible Hydrogen Storage. Part 2: Solid–State NMR Studies. J Phys Chem C 2011; 115: 6048–56.

[32] Garroni S, Milanese C, Pottmaier D, Mulas G, Nolis P, Girella A, et al. Experimental Evidence of $Na_2[B_{12}H_{12}]$ and Na Formation in the Desorption Pathway of the $2NaBH_4$+MgH_2 System. J Phys Chem C 2011; 115: 16664–71.

[33] MacKenzie KJD, Smith ME., ‘‘Multinuclear Solid State NMR of Inorganic Materials’’, Pergamon (2002).

[34] Wu X, Youngman RE, Dieckmann R. Sodium tracer diffusion and ^{11}B NMR study of glass of the type $(Na_2O)_{0.17}(B_2O_3)_x(SiO_2)_{0.83-x}$. J Non–Cryst Solids 2013; 378: 168–76.

[35] Wu J, Potuzak M, Stebbins JF. High–temperature in situ ^{11}B NMR study of network dynamics in boron–containing glass–forming liquids. J Non–Cryst Solids 2011; 357: 3944–51.

[36] Nielsen TK, Javadian P, Polanski M, Besenbacher F, Bystrzycki J, Skibsted J, et al. Nanoconfined $NaAlH_4$: prolific effects from increased surface area and pore volume. Nanoscale 2014; 6: 599–607.

[37] Kříž O, Čásenský B, Lyčka A, Fusek J, Heřmánek S. ^{27}Al NMR behavior of aluminium alkoxides. J Magn Reson 1969; 60: 375–81.

[38] Hwang SJ, Bowman Jr RC, Graetz J, Reilly JJ, Langley W, Jensen CM. NMR studies of the aluminium hydride phases and their stabilities. J Alloys Compd 2007; 446–447: 290–5.

Tables

Table 1

Nanoconfined samples	Amount of all components (wt. %)				Theoretical H_2 capacity (wt.%)
	PMMA-co-BM	MWCNT	$LiBH_4$	$NaAlH_4$	
$LiBH_4$-PcB	88.5	-	11.5	-	1.60
$LiBH_4$-PcB-MWCNT	91.9	0.1	8.0	-	1.10
$LiBH_4$-$NaAlH_4$-PcB	87.6	-	11.2	1.2	1.55

Table 2

Nanoconfined samples	Dehydrogenation temperature (°C)			Amount of gases desorbed with respect to H_2 content at 120 °C (%)						
	T_i	T_p	T_f	$•CH_3$	H_2O	CO	$•OCH_3$	CO_2	$•OC_4H_9$	Total
$LiBH_4$–PcB	80	105	135	13.4	0	6.9	0.8	16.3	26.9	64.3
$LiBH_4$–PcB–MWCNT	85	130	190	0.9	0.5	1.1	0.2	5.6	0.7	9.0
$LiBH_4$–$NaAlH_4$–PcB	95	125	165	1.0	2.8	1.1	1.3	1.1	0.6	7.9

T_i = Onset temperature
T_p = peak temperature
T_f = end temperature

Table 3

Nanoconfined samples	Peak area		υ(B–H)/υ(C=O) ratio
	υ(B–H) (2226-2386 cm^{-1})	υ(C=O) (1730 cm^{-1})	
$LiBH_4$–PcB	109.5	171.2	0.6
$LiBH_4$–PcB–MWCNT	12.2	4.5	2.7
$LiBH_4$–$NaAlH_4$–PcB	48.4	17.1	2.8

Figures

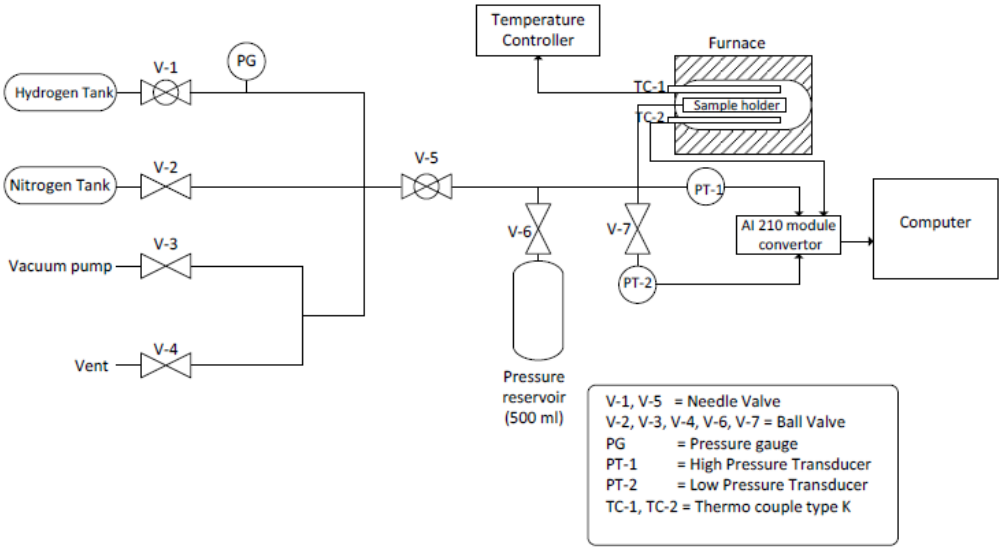

Figure 1

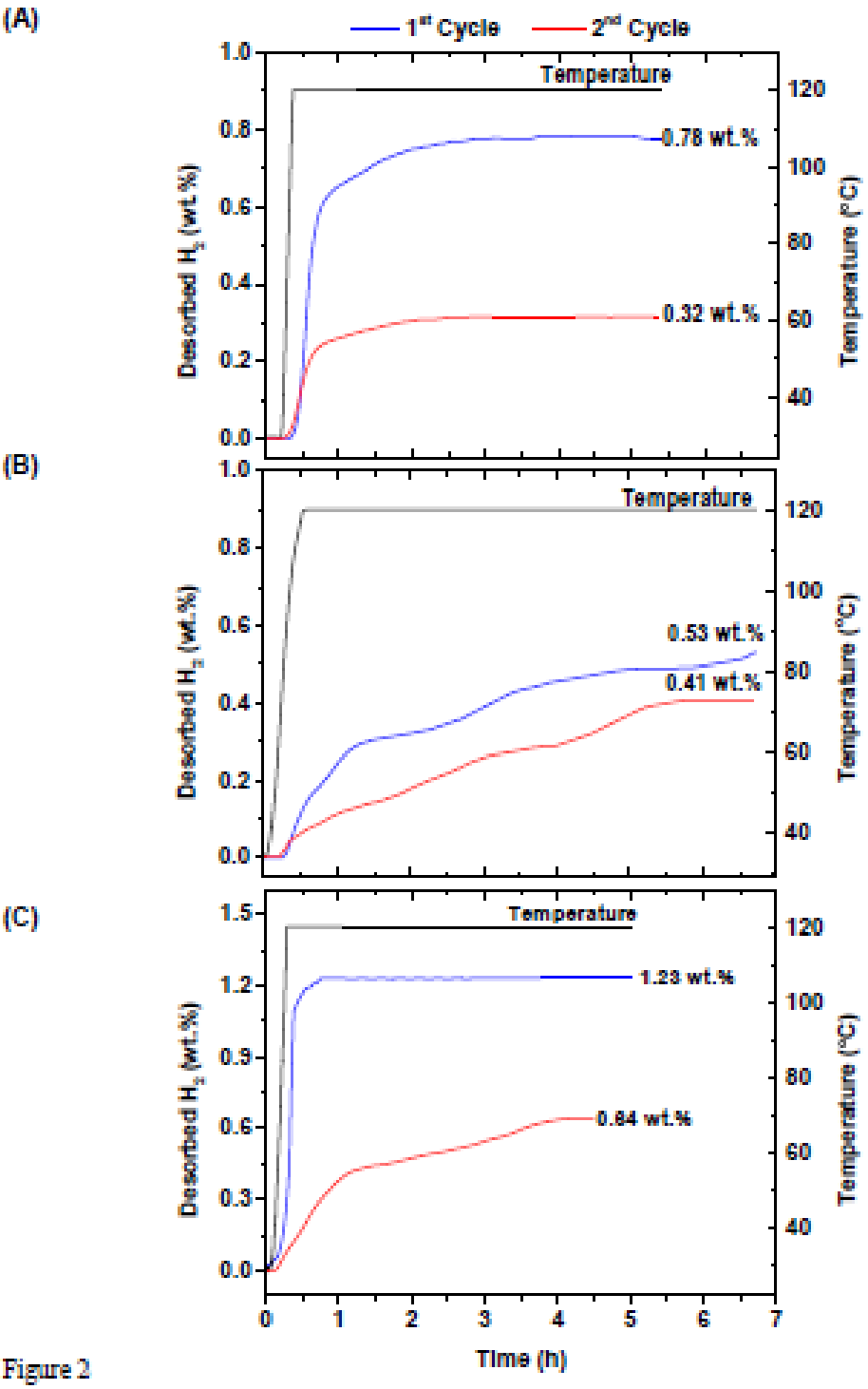
(A)
1st Cycle
2nd Cycle
Temperature
0.78 wt.%
0.32 wt.%
Desorbed H2 (wt.%)
Temperature (°C)
(B)
Temperature
0.53 wt.%
0.41 wt.%
Desorbed H2 (wt.%)
Temperature (°C)
(C)
Temperature
1.23 wt.%
0.84 wt.%
Desorbed H2 (wt.%)
Temperature (°C)
Time (h)

Figure 2

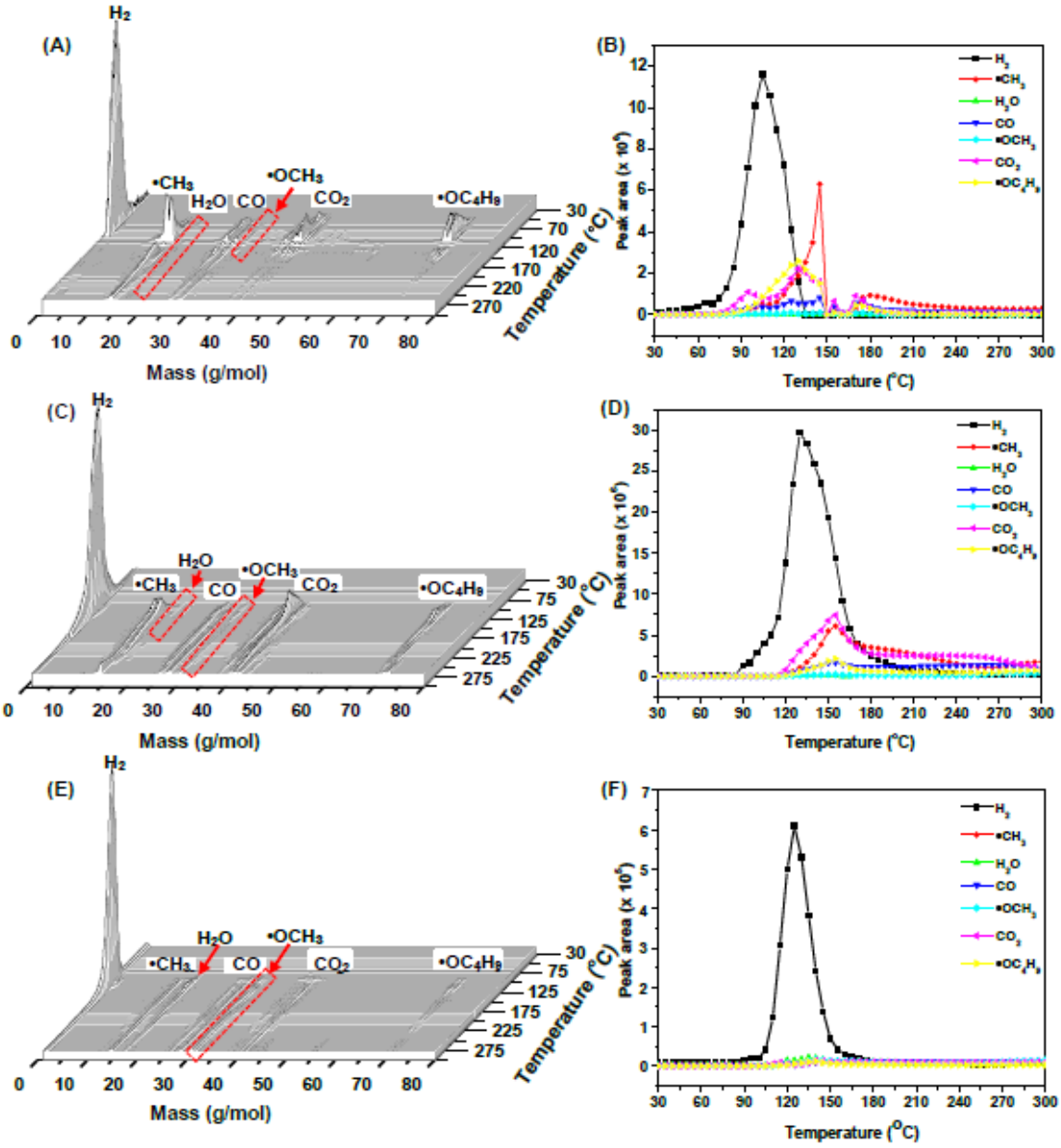
(A)
H2
•CH3
H2O
CO
•OCH3
CO2
•OC4H9
30
70
120
170
220
270
Temperature (°C)
0 10 20 30 40 50 60 70 80
Mass (g/mol)
(B)
Peak area (x 10⁶)
H2
•CH3
H2O
CO
•OCH3
CO2
•OC4H9
30 60 90 120 150 180 210 240 270 300
Temperature (°C)
(C)
H2
H2O
•CH3
CO
•OCH3
CO2
•OC4H9
30
75
125
175
225
275
Temperature (°C)
0 10 20 30 40 50 60 70 80
Mass (g/mol)
(D)
Peak area (x 10⁶)
H2
•CH3
H2O
CO
•OCH3
CO2
•OC4H9
30 60 90 120 150 180 210 240 270 300
Temperature (°C)
(E)
H2
H2O
•OCH3
•CH3
CO
CO2
•OC4H9
30
75
125
175
225
275
Temperature (°C)
0 10 20 30 40 50 60 70 80
Mass (g/mol)
(F)
Peak area (x 10⁶)
H2
•CH3
H2O
CO
•OCH3
CO2
•OC4H9
30 60 90 120 150 180 210 240 270 300
Temperature (°C)

Figure 3

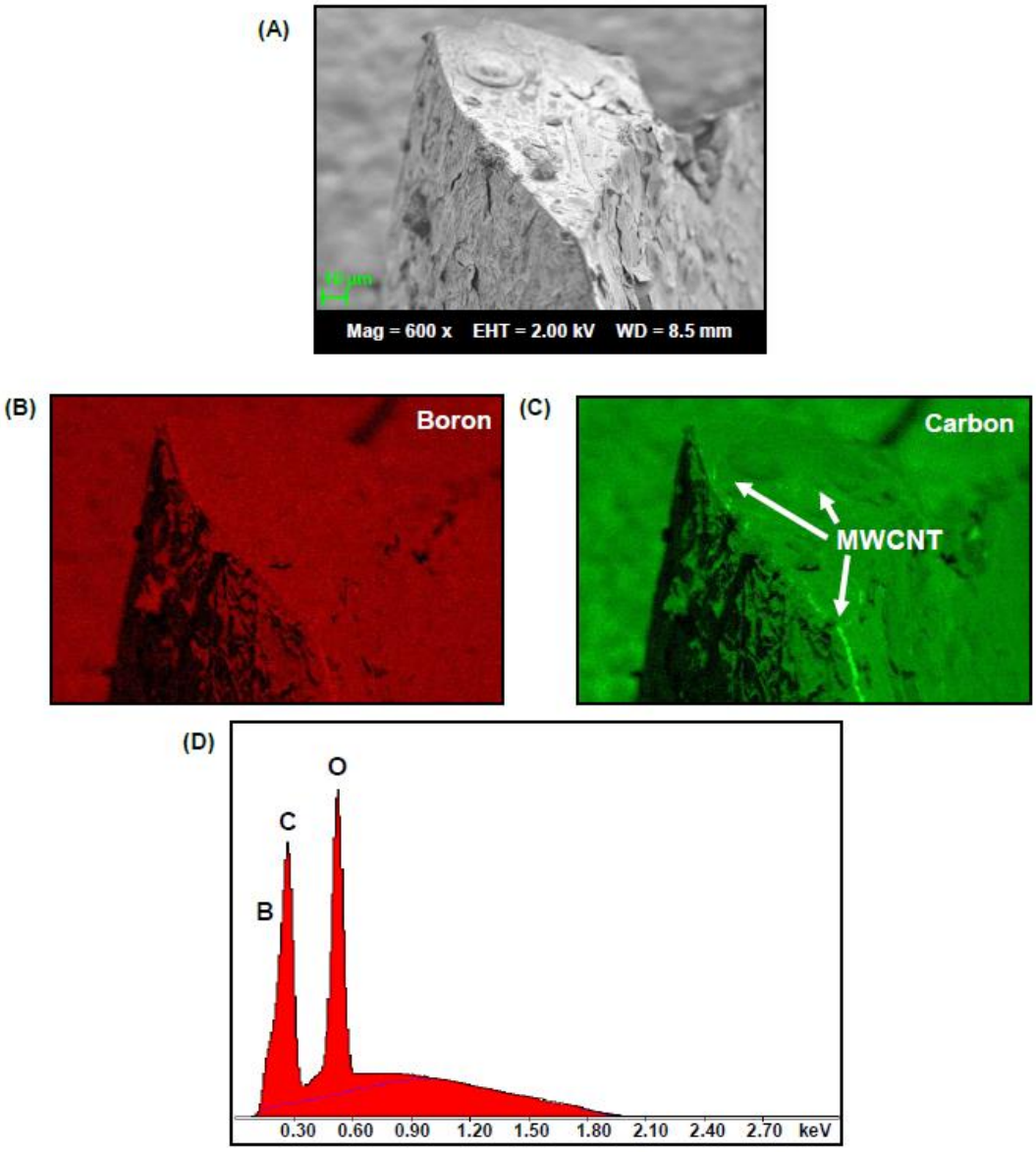
(A)
Mag = 600 x EHT = 2.00 kV WD = 8.5 mm
(B)
Boron
(C)
Carbon
MWCNT
(D)
O
C
B
0.30 0.60 0.90 1.20 1.50 1.80 2.10 2.40 2.70 keV

Figure 4

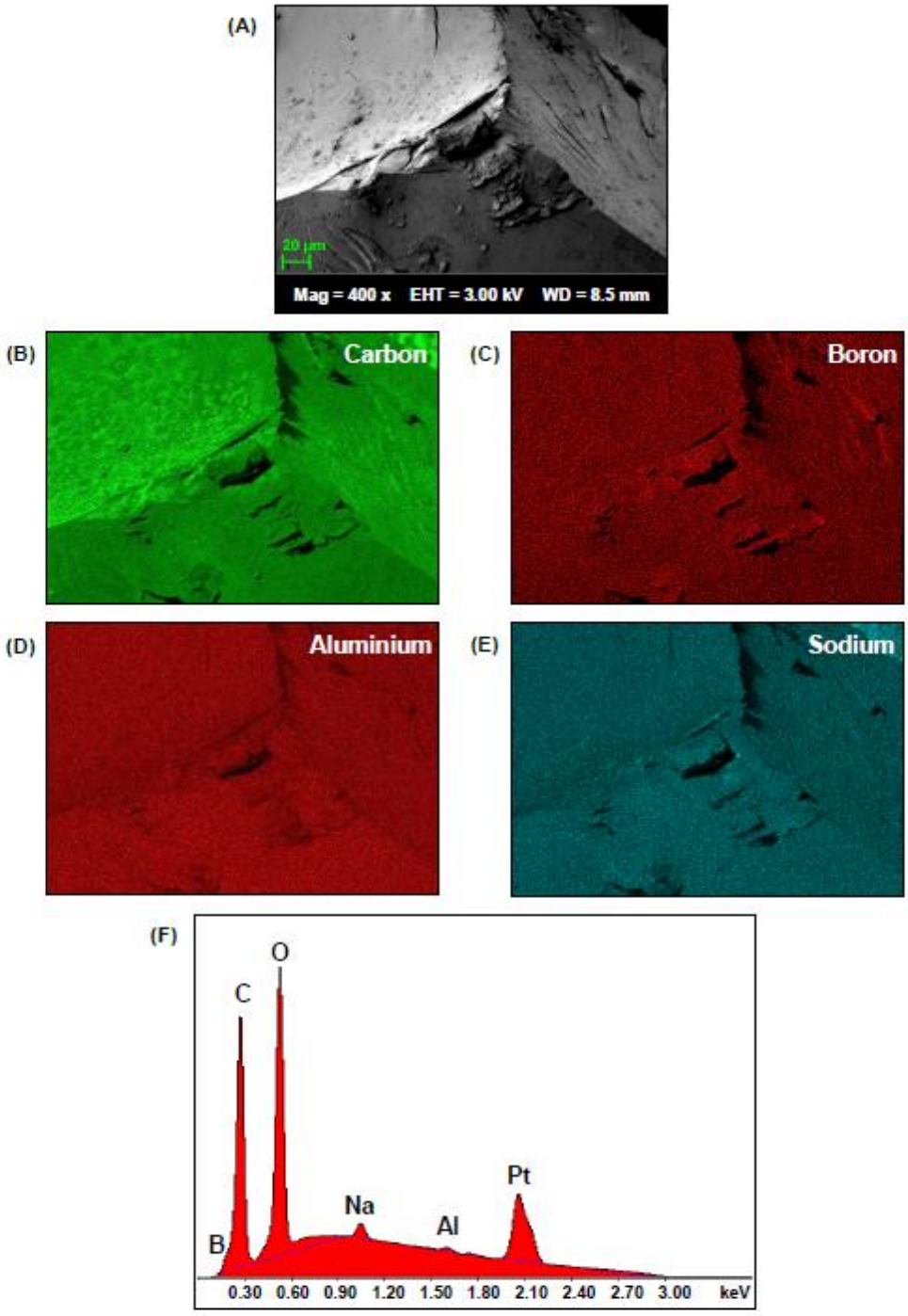
(A)
20 µm
Mag = 400 x EHT = 3.00 kV WD = 8.5 mm
(B)
Carbon
(C)
Boron
(D)
Aluminium
(E)
Sodium
(F)
O
C
Pt
Na
Al
B
0.30 0.60 0.90 1.20 1.50 1.80 2.10 2.40 2.70 3.00 keV

Figure 5

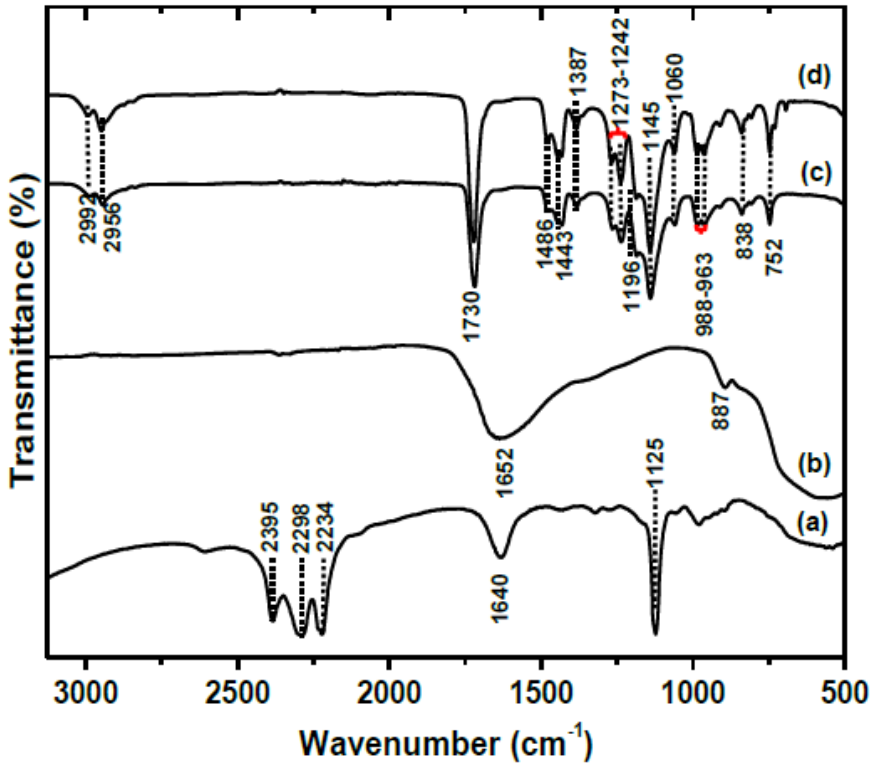
Transmittance (%)
Wavenumber (cm-1)
3000
2500
2000
1500
1000
500
(d)
(c)
(b)
(a)
2993
2956
1730
1486
1443
1387
1273-1242
1196
1145
1060
988-963
838
752
887
1652
1125
2395
2298
2234
1640

Figure 6

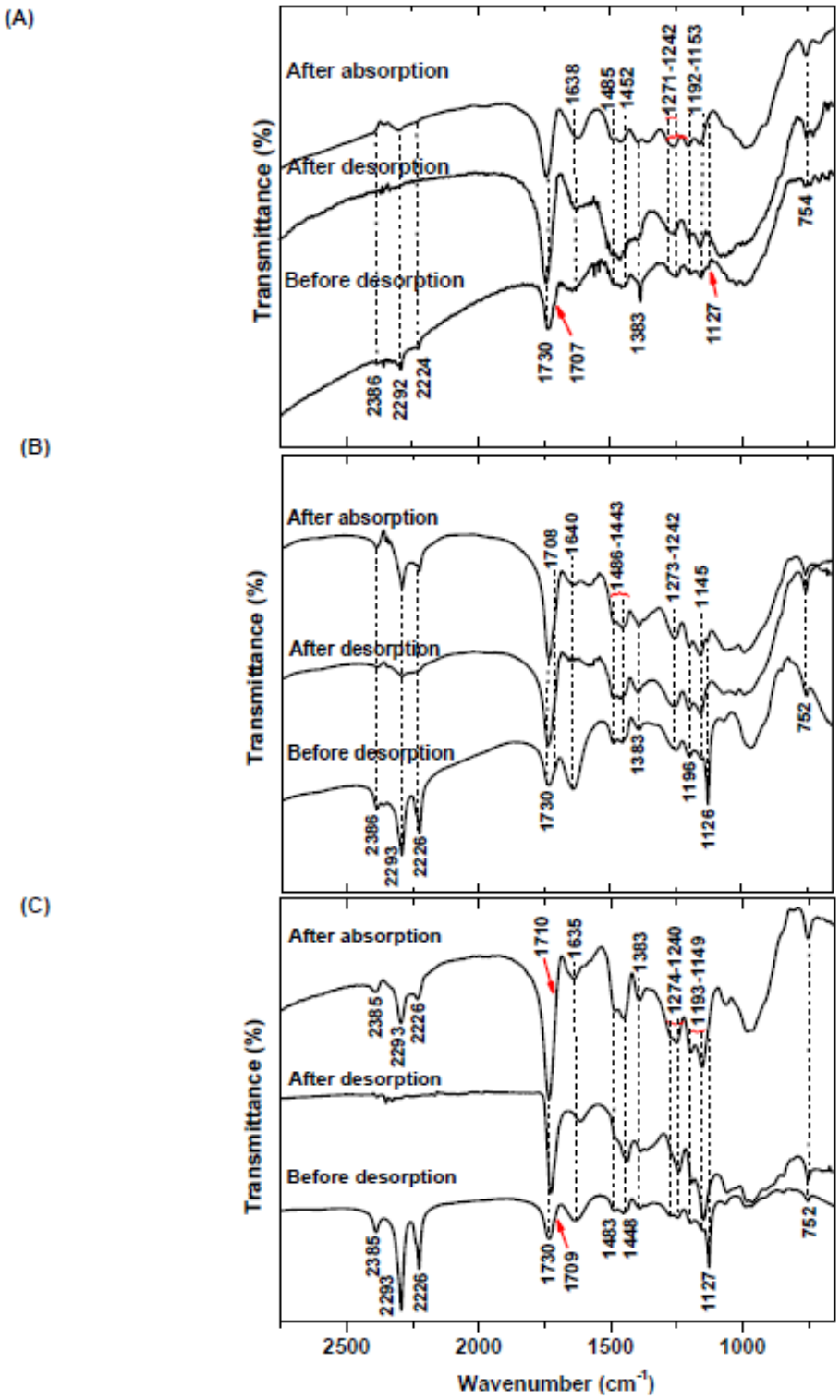
(A)
After absorption
After desorption
Before desorption
Transmittance (%)
2386
2292
2224
1730
1707
1638
1485
1452
1383
1271-1242
1192-1153
1127
754
(B)
After absorption
After desorption
Before desorption
Transmittance (%)
2386
2293
2226
1730
1708
1640
1486-1443
1383
1273-1242
1196
1145
1126
752
(C)
After absorption
After desorption
Before desorption
Transmittance (%)
2385
2293
2226
1730
1709
1710
1635
1483
1448
1383
1274-1240
1193-1149
1127
752
2500
2000
1500
1000
Wavenumber (cm-1)

Figure 7

(A)

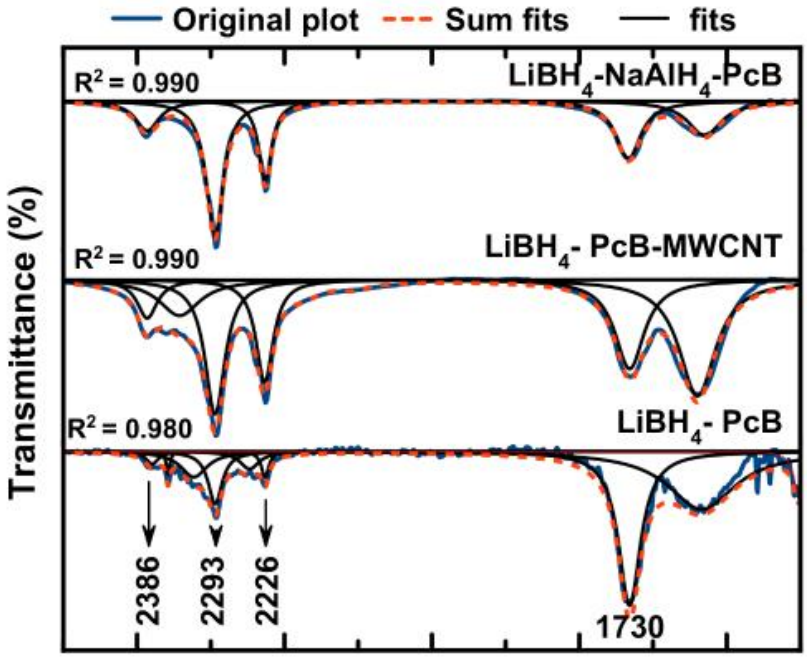
Original plot
Sum fits
fits
R² = 0.990
LiBH4-NaAlH4-PcB
R² = 0.990
LiBH4- PcB-MWCNT
R² = 0.980
LiBH4- PcB
Transmittance (%)
2386
2293
2226
1730

Figure 8

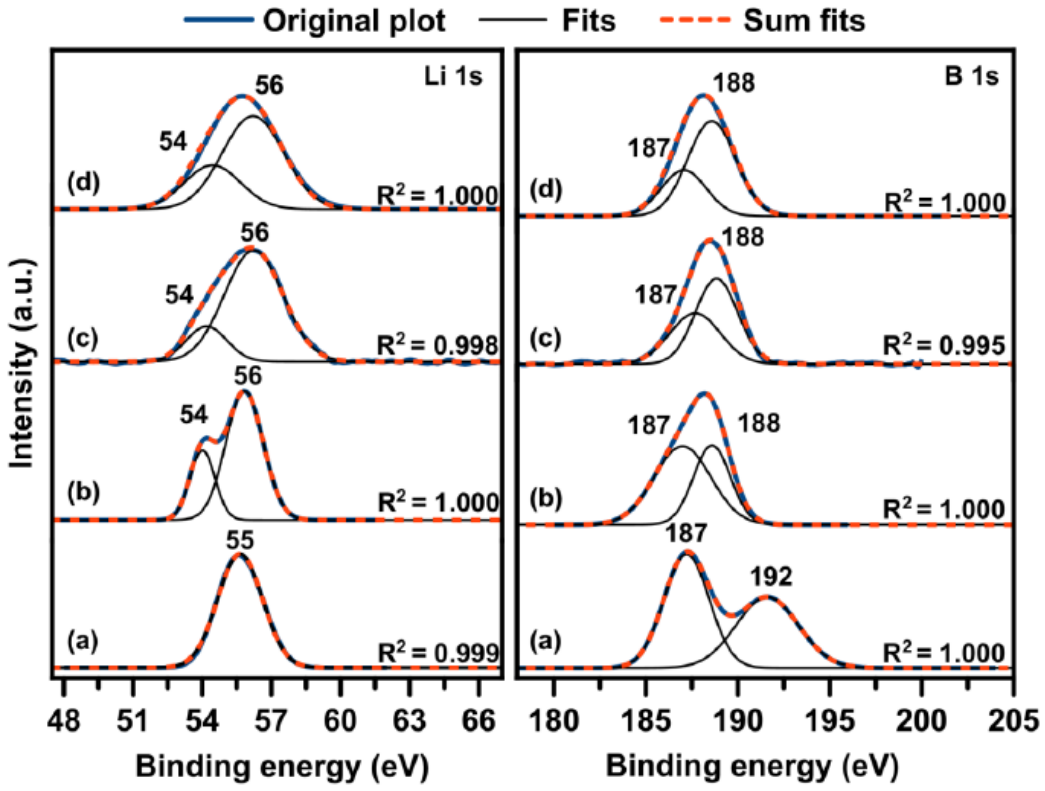
Original plot
Fits
Sum fits
Li 1s
B 1s
Intensity (a.u.)
(d)
(c)
(b)
(a)
56
54
55
188
187
192
R² = 1.000
R² = 0.998
R² = 0.999
R² = 0.995
48 51 54 57 60 63 66
180 185 190 195 200 205
Binding energy (eV)
Binding energy (eV)

Figure 9

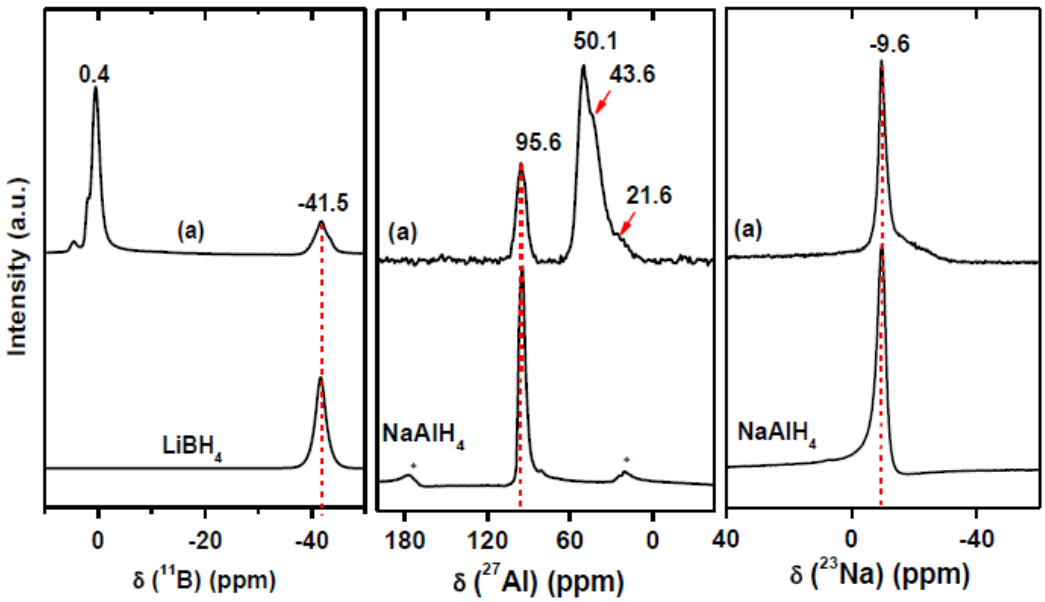
Intensity (a.u.)
0.4
-41.5
(a)
LiBH4
0
-20
-40
δ (11B) (ppm)
50.1
43.6
95.6
21.6
(a)
NaAlH4
180
120
60
0
δ (27Al) (ppm)
-9.6
(a)
NaAlH4
40
0
-40
δ (23Na) (ppm)

Figure 10